

Polarization entanglement with highly non-degenerate photon pairs enhanced by effective walk-off compensation method

Sungeun Oh* and Thomas Jennewein†

*Department of Physics and Astronomy, and Institute for Quantum Computing,
University of Waterloo, Waterloo, Ontario, Canada N2L3G1*

(Dated: May 14, 2024)

We demonstrate a novel entangled photon source (EPS) that produces polarization entanglement in highly non-degenerate photon pairs, generated through Type-0 spontaneous parametric down conversion (SPDC) using bulk periodically poled Lithium Niobate (PPLN). This source is specifically designed for entanglement-based quantum key distribution (EBQKD) between ground and satellite, as part of the Quantum Encryption and Science Satellite (QEYSSat) mission funded by the Canadian Space Agency (CSA). Through the utilization of birefringent beam displacers, a hybrid Mach-Zehnder a Sagnac interferometer, we ensure high polarisation contrast and stable interference of the highly non-degenerate photon pairs, which however causes substantial spatial and temporal walk-offs of the photon paths which poses a formidable challenge. We introduce an effective compensation method using birefringent crystal wedges to eliminate spatial and temporal walk-offs simultaneously. From only 1.0mW of pump power we observed a coincidence rate of $N = (33.33 \pm 0.05)\text{kHz}$, a significant improvement compared to the absence of the spatial compensation. We also observed an estimated pair generation rate of $(2.92 \pm 0.12)\text{MHz}$ and an entanglement visibility of $(96.6 \pm 0.3)\%$, making it a promising source for long-distance quantum communication for ground-to-satellite and fiber optic links.

I. INTRODUCTION

While numerous source for polarization entanglement with degenerate or near-degenerate photon pairs have been demonstrated[1–4], polarization entanglement with highly non-degenerate photon pairs has received less attentions. However, sources that produce highly non-degenerate photon pairs is relevant[5–8] in the context of quantum communication scenarios that require distinct wavelengths. Of our particular interest is the establishment of ground to space entanglement-based quantum key distribution (EBQKD)[9, 10], which necessitates a high pair production rate of around 100 MHz[11], as well as the utilization of connectivity to the satellite free-space link as well as to the ground-based optical fiber link. The photon to be transmitted through the ground-based optical fiber will preferably have a wavelength around 1550nm, to make it compatible with existing optical fiber infrastructure and make use of the low-loss transmission window. Photons with such a wavelength are most effectively received by superconducting nanowire single photon detectors (SNSPDs). However, because deploying SNSPDs on satellites is challenging due cryogenic cooling requirements [12], typically Silicon based single-photon avalanche diodes (SPADs) are chosen for a space based quantum receiver, such as in the QEYSSat payload. The Silicon-based photon detectors operate at a high performance and have been proven to operating in space[13–16]. As a result, the ground to space link will operate with a wavelength in the visible (VIS) or near-infrared (NIR) range for efficient photodetection. We

present an EPS specifically designed for implementing EBQKD between ground-based and satellite-based systems, as part of the Quantum Encryption and Science Satellite (QEYSSat) mission funded by the Canadian Space Agency (CSA)[17–19]. We implement a novel EPS system based on birefringent beam displacers and pairs of birefringent compensation wedges that generates photon pairs at the two distinct photon wavelengths. In particular, our novel compensation method effectively addresses the spatial and temporal walk-off of the photons caused by the birefringent beam displacer material and provides the degrees of freedom required to attain a high photon pair coupling as well as high entanglement quality in our EPS.

II. SCHEME TO GENERATE POLARIZATION ENTANGLED NON-DEGENERATE PHOTON PAIRS

Our EPS generates photon pairs through spontaneous parametric down conversion (SPDC)[20] in optically non-linear crystals. A continuous wave (CW) laser (Frankfurt laser, Germany) provides a polarized pump beam at a wavelength of $\lambda_p = 523.6\text{nm}$, with a bandwidth of $\Delta\lambda_p = 0.1\text{nm}$. A 10mm long Type-0 PPLN crystal (Covesion, UK) with a poling period of $\Lambda = 7.1\mu\text{m}$ (at room temperature), converts pump(p) photons into signal(s)-idler(i) photon pairs with the same polarization under the following quasi-phase matching (QPM) conditions:

$$\frac{2\pi}{\Lambda(T)} = k_p - k_s - k_i \quad (1)$$

$k = 2\pi n(\lambda, T)/\lambda$ are the wave vectors, where $n(\lambda, T)$ are the wavelength- and temperature-dependent refractive

* SungeunOh68@gmail.com

† thomas.jennewein@uwaterloo.ca

indices of the crystals for the corresponding fields. The reason for the crystal choice is that PPLNs can achieve a higher photon pair generate rate compared to other conventional nonlinear crystals, due to its high nonlinear coefficient[21]. With the presented values, we obtain signal photons at a wavelength of $\lambda_s = 790.8nm$ suitable for free-space transmission, and idler photons at a wavelength of $\lambda_i = 1550nm$ suitable for ground transmission through optical fiber. The associated spectral bandwidths $\Delta\omega$ (at 1/e) are estimated by the first-order Taylor expansion of equation 1.

$$\Delta k \approx \left. \frac{\partial k_p}{\partial \omega} \right|_{\omega_p} \Delta\omega_p - \left. \frac{\partial k_s}{\partial \omega} \right|_{\omega_s} \Delta\omega_s - \left. \frac{\partial k_i}{\partial \omega} \right|_{\omega_i} \Delta\omega_i = \frac{2\pi}{L} \quad (2)$$

Using equation 2, the temporal widths $\tau = 2\pi/\Delta\omega$ (at 1/e) are $\tau_s = 2.68$ ps for the signal photon, and $\tau_i = 2.61$ ps for the idler photon. We consider entanglement of signal and idler photons with horizontal (H) and vertical (V) polarizations using an optical interferometer. The resulting Bell state can be written as

$$|\text{Bell}\rangle = \frac{1}{\sqrt{2}} \left(|V_s V_i\rangle + e^{i(\phi_r + \Delta\phi_r)} |H_s H_i\rangle \right) \quad (3)$$

The overall relative phase between the $|VV\rangle$ and the $|HH\rangle$ states can be represented as a combination of the relative phase resulting from the path difference (denoted as ϕ_r) and the relative phase variation induced by temperature fluctuations in optical components, contributing to the additional difference in paths (denoted as $\Delta\phi_r$). For instance, maximal entanglement in the linear diagonal polarization is achieved when the overall phase $\Delta\phi_r = 0$. The phase variation from each beam path in the interferometer due to thermal and other fluctuations becomes $\Delta\phi = \delta\phi_p + \delta\phi_s + \delta\phi_i$, where each term is

$$\delta\phi = \sum_j \frac{2\pi L_j}{\lambda} \left(\frac{\partial n_j}{\partial T} + n_j \alpha \right) \Delta T, \quad (4)$$

representing the phase shift introduced by all transmissive optical components, each indexed with j , within the interferometer, each with a length of L_j . The thermo-optic coefficients $\partial n_j/\partial T$ and the thermal expansion coefficient α inside the bracket in equation 4 correspond to the changes in the refractive index and the material length, respectively. One interferometer design widely used for quantum entanglement generation is the Sagnac interferometer, which incorporates self-compensation for relative phase stabilization [8]. However, a Sagnac interferometer with a polarization beamsplitter, which is commonly used, has technical difficulties in achieving entanglement in non-degenerate photon pairs with high-efficiency transmission for both signal and idler photons, while simultaneously accommodating their two orthogonal polarizations. The reason lies in the wavelength dependency of the transmittivity and reflectivity ratio of the polarization beamsplitter [22].

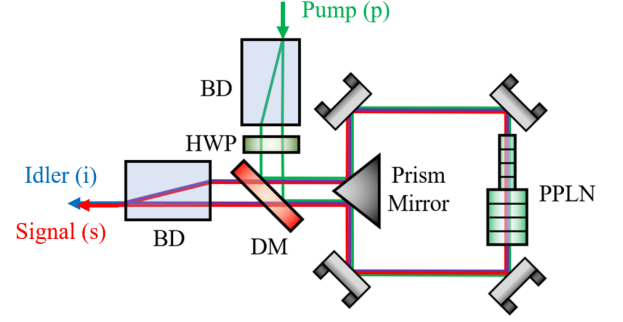


FIG. 1: Schematic diagram of the interferometer implementing two beam displacers and a half waveplate and including Sagnac loop. Two PPLN crystals are placed in the loop, each responsible for the SPDC of one of the polarized pump beams.

To overcome this challenge, we chose to build an optical interferometer employing two birefringent beam displacers capable of splitting and recombining two orthogonally polarized beams, and inserting a half waveplate (HWP) between the two beam displacers in order to have two identical path lengths [23–25]. Thereby the beam that was originally an ordinary ray (non-deflected, denoted with subscript 'o') and the extraordinary ray (deflected ray, denoted with subscript 'e') switch roles as their polarizations are interchanged. Hence, this scheme allows for the effective transmissions of all three waves through the interferometer. The perfect alignment of the two beam displacers can be seen as an equivalent configuration to the Sagnac interferometer, but this is always an ideal case. To ensure self-phase compensation, we add an actual Sagnac loop into the interferometer, by inserting a dichroic mirror along the beam path between the half waveplate and the second beam displacer. This way, the dichroic mirror reflects the two orthogonally polarized pump beams, allowing them to enter the Sagnac loop, and transmits the signal and idler beams with both polarizations effectively. Another advantage of including the Sagnac loop is the prevention of back reflection from the interferometer to the pump laser. If we solely apply the beam-displacing interferometer scheme, the returning pump beam, which has not undergone down-conversion, will be recombined at the first beam displacer through the same beam paths. However, with the presence of the additional Sagnac loop, the beam disperses upon returning to the first beam displacer, eliminating the risk of laser instability or even damage.

The phase variation of each of the separated beam paths along the Sagnac loop (denoted with subscripts, CW (clock-wise) and CCW (counter clock-wise)) is expressed as follows.

$$\begin{aligned} \Delta\phi_{CW} &= \delta\phi_e(\lambda_p, T) + \delta\phi_o(\lambda_s, T) + \delta\phi_o(\lambda_i, T) \\ \Delta\phi_{CCW} &= \delta\phi_o(\lambda_p, T) + \delta\phi_e(\lambda_s, T) + \delta\phi_e(\lambda_i, T) \end{aligned} \quad (5)$$

The relative phase variation is then

$$\begin{aligned} \Delta\phi_r &= \Delta\phi_{CW} - \Delta\phi_{CCW} \\ &= \delta\phi_r(\lambda_p, T) - \delta\phi_r(\lambda_s, T) - \delta\phi_r(\lambda_i, T) \end{aligned} \quad (6)$$

where $\delta\phi_r = \delta\phi_e - \delta\phi_o$. We make the assumption that the phases introduced by the half waveplate and the dichroic mirror are negligible in comparison to those induced by the beam displacers, due to their much smaller thicknesses. Phase variations are then calculated to be $\delta\phi_r(\lambda_p, T) = 6.22\pi$, $\delta\phi_r(\lambda_s, T) = 4.09\pi$ and $\delta\phi_r(\lambda_i, T) = 2.08\pi$. Hence, the relative phase is $\Delta\phi_r = 0.052\pi$, ensuring sufficient phase stability. No self-compensation effect would introduce a phase shift of $\Delta\phi_r = 12.39\pi$. As a result, while self-compensation may not be entirely perfect, it certainly helps quantum states remain usable for a longer period of time.

III. SPATIOTEMPORAL WALK-OFF COMPENSATION

Achieving a high entangled photon pair generation rate requires high spatial and temporal (phase) overlap of both the signal beams and the idler beams. Even if the relative phase (ϕ_r in equation 3) is minimized to some extent in the Sagnac loop of our source, there is still phase introduced by the two beam displacers. The amount of displacement of the extraordinary ray in the beam displacers can be determined from its angle of refraction, denoted as θ_e . This angle can be obtained from the refractive indices of the ordinary and extraordinary rays (denoted as n_o and n_e , respectively), and the optic angle (angle between the optic axis and the axis normal to the surface of the medium for the incident rays, denoted as θ) of the material.

$$\tan \theta_e = \left(1 - \frac{n_o^2}{n_e^2}\right) \frac{\tan \theta}{1 + \frac{n_o^2}{n_e^2} \tan^2 \theta} \quad (7)$$

It is worth noting that equation 7 assumes the incident beam entering the medium perpendicular to the surface of the medium. The separation between the two rays created by the beam displacer with a length of L is then $D = L \tan \theta_e$. When the down-converted signal and idler photons pass through the second beam displacer, they do not return to their original position, given that their wavelengths are no longer the pump wavelength. This deviation from the original position is referred to as spatial walk-off, denoted as ΔD .

$$\Delta D_{s,i} = L \tan \theta_{e,2}^p - L \tan \theta_{e,1}^{s,i} \quad (8)$$

$\theta_{e,1}$ and $\theta_{e,2}$ are the refraction angles of the first and the second beam displacers, respectively, as shown in Figure 2. We use two identical α BBO beam displacers (Newlight Photonics inc, Canada) with the lengths

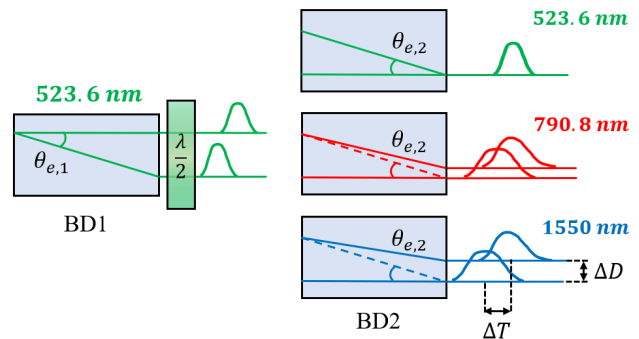


FIG. 2: Diagrams illustrating how the signal and idler beams undergo spatial ΔD and temporal ΔT walk-offs in the second beam displacer. If the beams had maintained the pump wavelength, then no walk-off would have occurred at the second beam displacer. The degree of displacement decreases as the wavelength increases.

of $L = 39.4$ mm for the interferometer. According to equation 8, the spatial walk-offs of the signal and the idler beams are 0.10 mm and 0.17 mm, respectively. The time taken for the beam to pass through the beam displacer can be easily conceptualized through a geometric approach.

$$T_{o \rightarrow e}^{s,i} = \frac{\mathcal{N}_o^p L}{c} + \frac{\mathcal{N}_e^{s,i} L}{c \cos \theta_{e,2}^{s,i}} \quad (9)$$

$$T_{e \rightarrow o}^{s,i} = \frac{\mathcal{N}_e^p L}{c \cos \theta_{e,1}^p} + \frac{\mathcal{N}_o^{s,i} L}{c}$$

$T_{o \rightarrow e}$ is the time taken by the ray, which initially travels straight and then becomes displaced. Similarly, $T_{e \rightarrow o}$ is the time taken by the ray, which initially becomes displaced then travels straight. \mathcal{N}_o and \mathcal{N}_e are group indices of the o-ray and e-ray, respectively. The temporal walk-off is then the time difference between the two travel time.

$$\Delta T_{s,i} = T_{o \rightarrow e}^{s,i} - T_{e \rightarrow o}^{s,i} \quad (10)$$

Using equation 10, we obtain the temporal walk-offs of 0.65 ps for the signal beam and 1.06 ps for the idler beam. Both spatial and temporal walk-offs not only reduce the entangled photon pair rate but also degrade the entanglement visibility, and this worsens with more extreme degenerate photon pairs. Employing birefringent materials to compensate for the temporal walk-offs is a commonly used method. Here, we additionally employ a separation between two birefringent crystal wedges, allowing simultaneous compensations for both spatial and temporal walk-offs. The choice of a wedge shape offers several advantages. As illustrated in Figure 3 one side is flat, allowing the ray to enter perpendicularly. This simplifies calculations for group indices appearing in equation

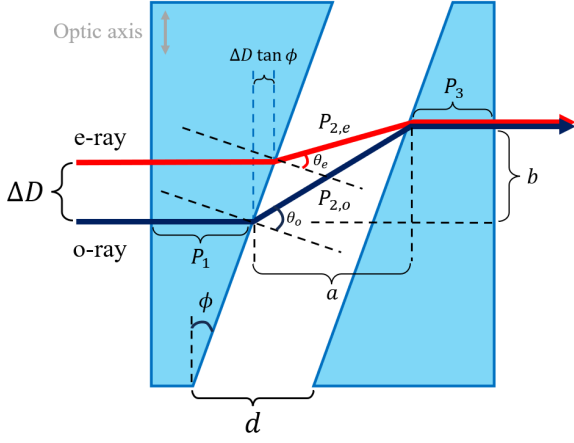


FIG. 3: Schematic diagram of two Calcite wedges used to compensate for both spatial and temporal walk-offs. The optic axis of our Calcite wedges is aligned perpendicular to the direction of ray propagation such that both the ordinary (purple) and extraordinary (red) rays undergo no beam displacement when entering the Calcite perpendicularly. However, upon exiting the first wedge, the e-ray experiences more refraction than the o-ray due to negative birefringence ($n_e < n_o$). The path lengths of the e-ray and the o-ray in between the two wedges are shown as $P_{2,e}$ and $P_{2,o}$, respectively.

9. Moreover, even if the ray exits the first wedge at a non-perpendicular angle, when it enters the second wedge that is identical in shape, it regains its original propagation direction. For our source, we use Calcite as birefringent wedges to slow down the o-rays. A wedges angle $\phi = 15^\circ$ is chosen arbitrarily. Since Calcite is a negative uniaxial material, o-rays experience more refraction than the e-rays, in both the signal and the idler path. It is worth noting that in the first Calcite wedge (on the left), the e-ray travels a slightly longer distance than the o-ray by $\Delta D \tan \phi$. Also, when a gap between the two crystal wedges is introduced, the distance the two beams travel within the gap is slightly different, due to the different bendings of the paths. Consequently, the o-ray travels a longer distance than the e-ray, resulting in a reduction of the temporal walk-off. This leads to either an increase or a decrease in the original temporal walk-off, and all of these should be taken into account when determining the thickness of the crystal. By identifying the correct lateral separation (shown as d in Figure 3) between the two wedges, we effectively merge the two rays at the second wedge, compensating for the spatial walk-offs. At the same time, temporal walk-offs can easily be compensated by the thickness of the wedges.

We determine the lateral separation d needed between the wedges for a perfect spatial overlap. The vertical displacement of the o-ray is $b = a \tan(\theta_o - \phi)$ such that the vertical shift of the e-ray is $b - \Delta D$. In doing so, a relationship between the two vertical displacements can

be established as follows.

$$a \tan(\theta_o - \phi) - \Delta D = (a - \Delta D \tan \phi) \tan(\theta_e - \phi) \quad (11)$$

$\theta_{o,e}$, ϕ and ΔD are known quantities, so we can rearrange equation 11 to determine a .

$$a = \frac{1 - \tan \phi \tan(\theta_e - \phi)}{\tan(\theta_o - \phi) - \tan(\theta_e - \phi)} \Delta D \quad (12)$$

Finally, we calculate the lateral separation d as follows.

$$d = a - b \tan \phi \quad (13)$$

The total path lengths for each ray can be expressed as follows.

$$P(\text{o-ray}) = P_1 + P_{2,o} + P_3 \quad (14)$$

$$P(\text{e-ray}) = P_1 + \Delta D \tan \phi + P_{2,e} + P_3$$

The difference in travel times between the two paths is then

$$\Delta T = \left[\frac{n_o}{c} (P_1 + P_3) + \frac{1}{c} P_{2,o} \right] - \left[\frac{n_e}{c} (P_1 + \Delta D \tan \phi + P_3) + \frac{1}{c} P_{2,e} \right] \quad (15)$$

By setting the overall thickness of the wedges to

$$L = \frac{c \Delta T}{|n_e - n_o|} = \frac{(\mathcal{N}_o - \mathcal{N}_e) (P_1 + P_3) + P_{2,o} - P_{2,e} - \mathcal{N}_e \Delta D \tan \phi}{|n_e - n_o|} \quad (16)$$

we can effectively cancel out the temporal walk-off. To mention again, all derivations take into account compensations involving negative birefringent wedges (one can derive for positive birefringent wedges in a similar manner).

The less overlap between the two beams, the higher the relative phase in equation 3. If we already know the ideal photon pair rate (representing perfect beam overlap), we can intuitively analyze the impact of spatial and temporal walk-offs by multiplying the ideal photon rate with a beam overlap factor. We consider Gaussian fields and characterize the spatial modes of the ordinary and extraordinary rays.

$$g(x, y) = \frac{1}{\sqrt{2\pi\sigma^2}} e^{-(x^2+y^2)/2\sigma^2} \quad (17)$$

The standard deviation can be obtained from the full-width-half-maximum, $\text{FWHM} = 2\sqrt{2 \ln 2} \sigma$. The spatial overlap of the two beam separated by ΔD is then the product of the two Gaussians integrated over the transverse plane (x,y) as follows.

$$\int_{-\infty}^{\infty} g_o(x, y) g_e(x - \Delta D_x, y - \Delta D_y) dx dy \quad (18)$$

The temporal overlap can be determined in a similar manner, using equation 17 for the temporal modes of the ordinary and extraordinary rays. The standard deviation can be derived from the temporal width $\tau = 2\sqrt{2\ln 2}\sigma$.

IV. EXPERIMENTS AND RESULTS

We demonstrate polarization-entanglement of photons with our entangled photon source, with the hybrid interferometer implemented (as shown in Figure 4). The

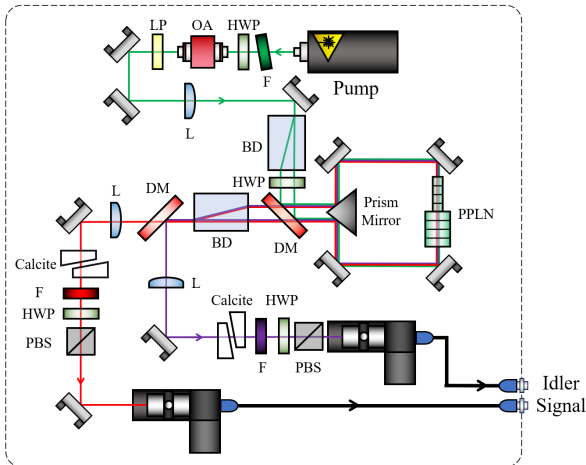


FIG. 4: Design of the EPS. The optical components are : Filter (F), Optical Isolator (OA), Linear Polarizer (LP), Lens (L), Beam Displacer (BD), Half waveplate (HWP), Dichroic Mirror (DM), Polarizing Beam splitter (PBS)

pump beam collimated by an aspheric lens ($f_p = 8$ mm) passes through several optical components to be diagonally polarized. It is then focused by the magnifying lens ($f_p = 40$ cm) to the PPLN crystals in the Sagnac loop. The first beam displacer splits the diagonally polarized pump beam into two beams with horizontal and vertical polarization by displacing one of them that is extraordinary with respect to the displacer's optic axis. The polarization of the two beams is switched by passing through a half waveplate before they enter the Sagnac loop. The first dichroic mirror reflects the pump beam into the Sagnac loop, while allowing the signal and idler beams that are produced from down conversion by the PPLN crystals to pass through and reach the second beam displacer. We place two identical PPLN crystals perpendicular to each other such that one is responsible for $|o\rangle_p \rightarrow |o\rangle_s |o\rangle_i$ while the other is responsible for $|e\rangle_p \rightarrow |e\rangle_s |e\rangle_i$. The two signal and idler beams combined by the second beam displacer are separated by the second dichroic mirror (signal beam is transmitted and idler beam is reflected). Along each beam path, there is another lens ($f_s = 60$ cm and $f_i = 50$ cm) to re-collimate the beam before entering the Calcite wedges

for the walk-off compensation. It is worth noting that the lenses are placed before the wedges in order to prevent from the beam entering non-perpendicular to the wedges' surfaces. At this point, we would expect the signal and the idler photons to be completely entangled. A long-pass filter and a bandpass filter are placed on each beam path to ensure that any noises are reduced. The polarization-entanglement test is proceeded by measuring the polarization correlation of the Bell states. A half-wave plate and a polarizing beam splitter are placed on the end of each beam path (signal and idler). The arrived signal and idler photons are focused by the aspheric lenses ($f_s = 11$ cm and $f_i = 15$ cm) and collected through the SMFs. SPAD (Exceltilas, USA) and SNSPD (Quantum Opus, USA) are used to collect signal and idler photons, respectively. The detection efficiencies from the signal and the idler beam paths are estimated to be $\eta_s = 0.38$ and $\eta_i = 0.217$ considering all the optical components along the ways including the detectors (These values are estimated based on the specifications of the optical components provided by the manufacturers). The coincidence counts within a 1.5 ns detection window are measured using a time-tagging unit. In actual experiments, higher values of $\Delta D_s = 0.145$ mm and $\Delta D_i = 0.325$ mm are observed due to additional divergence at the two dichroic mirrors. Nevertheless, compensating for the spatial walk-off should pose no issues with the additional divergence and should simply be taken into account. By scanning the beams in the transverse directions with our detectors, we identify the FWHM of the signal and idler beams at the receiving fibers to be 0.6 mm and 0.8 mm, respectively. With the actual walk-offs obtained from the experiment, the spatial overlap factors calculated from equation 18 are 52.4% for the signal photon, and 17.1% for the idler photon. Using equation 13, the lateral separation needed for the signal and idler paths are calculated to be $d_s = 2.75$ mm and $d_i = 6.6$ mm, respectively. To validate our compensation for the spatial walk-off, the lateral separation between the wedges on the idler side is varied as 0 mm, 1.6 mm, 3.6 mm, 6.6 mm, 9.6 mm and 11.6 mm, while the spatial walk-off on the signal side is fully compensated (see Figure 5a). With the pump power of 1.0 mW, background subtracted coincidence counts at each variation is measured and plotted on Figure 5b. The peak experimental value plotted on the idler graph corresponds to when spatial walk-off is fully compensated for both the signal and idler beams, with the coincidence counts measuring $N = (33.33 \pm 0.05)$ kHz. This marks almost eight times enhancement in the coincidence counts, as without compensation on the idler side (while the signal side remained fully compensated), the coincidence count was $N = (4.20 \pm 0.01)$ kHz. The additional beam divergence (resulting in spatial walk-off) did introduce some ambiguities when determining temporal walk-off compensation. If we neglect any additional temporal walk-offs other than those caused by the beam displacers, the temporal overlaps of two Gaussian intensity profiles, as calculated using

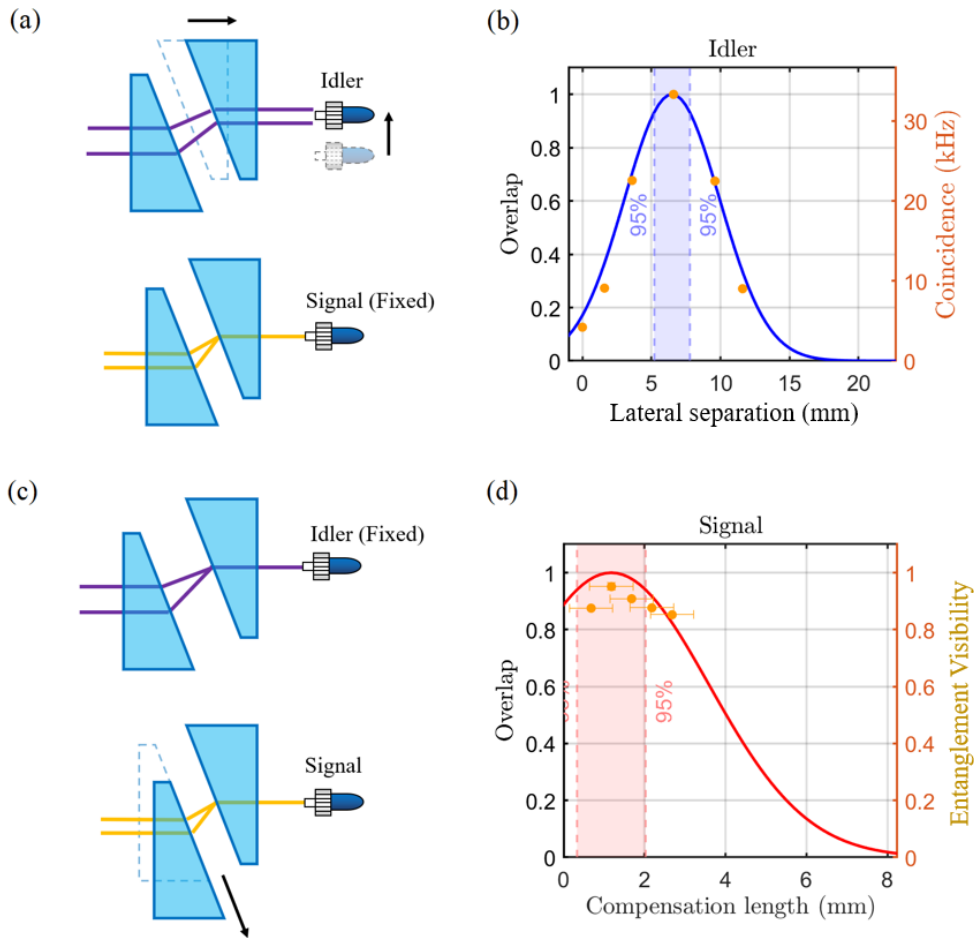


FIG. 5: (a) Spatial walk-off compensation. While fixing the signal side (fully compensated), we shift the position of one of the Calcite wedges on the idler side, as shown in the diagram, varying the gap. The optical fiber collecting idler photons is realigned, and the thickness is simultaneously corrected for each gap variation. (b) Theoretical curve of the spatial overlap for idler photons (solid line) as a function of lateral separation, along with the calculated coincidences (dot) for each lateral separation. Note that both the vertical and horizontal error bars are too short to be visible. (c) Temporal walk-off compensation. While fixing the idler side (fully compensated), we shift the position of one of the Calcite wedges on the signal side, as shown in the diagram, varying only the thickness. (d) Theoretical curve of the temporal overlap for signal photons (solid line) as a function of compensation length, along with the calculated visibility (dot) for each compensation length. Note that the vertical error bars are too short to be visible.

temporal version of equation 18, are 88.8% for the signal photon, and 72.1% for the idler photon. To validate our compensation for the temporal walk-off, the compensation length (the overall thickness of the wedges) on the signal side is varied as 0.68 mm, 1.18 mm, 1.68 mm, 2.18 mm and 2.68 mm (see Figure 5c). The values are chosen simply to plot the entanglement visibility with its optimal value centered on the graph shown in Figure 5d. The correlations are measured by rotating the half waveplate on the signal arm while the half waveplate on the idler arm are fixed to 0° (V basis), 45° (A basis), 90° (H basis) and 135° (D basis). Then the visibility $V = (N_{c,max} - N_{c,min}) / (N_{c,max} + N_{c,min})$ of each of the four bases is obtained from the minimum and maximum

coincidence counts of the correlation measurements. The result shows the peak average value of $V = (96.6 \pm 0.3)\%$, clearly showing the enhancement in the entanglement visibility by the Calcite wedges. Furthermore, based on the compensation results, the additional beam divergence appears to have had minimal, if any, impact on the trend.

Figure 6 shows the optimal entanglement test results. The measured visibilities with the full walkoff compensation are $V = (96.8 \pm 0.5)\%$, $V = (95.5 \pm 0.5)\%$, $V = (98.6 \pm 0.5)\%$ and $V = (95.4 \pm 0.5)\%$. In order to confirm the entanglement, we perform the CHSH test

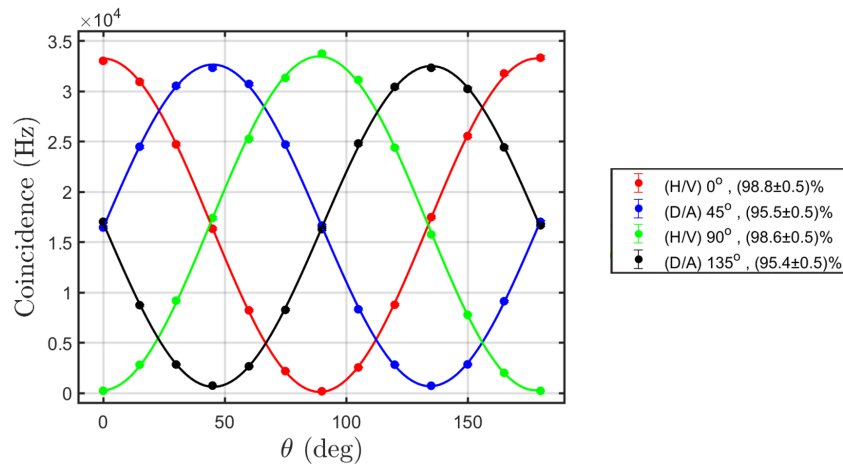


FIG. 6: Polarization entanglement measurement results. The correlation measurement was conducted using four different polarization bases. The coincidence counts, measured at 1.0 mW of pump power while changing the polarization angle from 0° to 180° , are plotted on the graph.

[26]. The CHSH inequality is expressed as

$$S = |E_{\alpha,\beta} - E_{\alpha,\delta} + E_{\gamma,\delta} + E_{\gamma,\beta}| \leq 2 \quad (19)$$

where we have the correlation estimates expressed as

$$E_{\alpha,\beta} = \frac{N(\alpha, \beta) - N(\alpha, \beta^\perp) - N(\alpha^\perp, \beta) + N(\alpha^\perp, \beta^\perp)}{N(\alpha, \beta) + N(\alpha, \beta^\perp) + N(\alpha^\perp, \beta) + N(\alpha^\perp, \beta^\perp)} \quad (20)$$

Here, we define additional angles, $\alpha^\perp = \alpha + 90^\circ$ and $\beta^\perp = \beta + 90^\circ$. We chose $\alpha = 0^\circ$, $\beta = 22.5^\circ$, $\gamma = 45^\circ$ and $\delta = 67.5^\circ$ and confirmed that the inequality is strongly violated at $S = 2.75 \pm 0.03$ by 25 standard deviations, which also agrees nicely with the expected value from the average visibility $S_{exp} = 2\sqrt{2}V_{avg} \approx 2.75$, indicating the quantum entanglement [26, 27]. We also examine the consistency of experimental data quality with increasing pump power levels. The experimental data includes the single counts of signal (N_s) and idler (R_i) photons, as well as coincidence counts (N) representing simultaneous detection of the signal and the idler photons. The results are plotted in Figure 7a. At a pump power of 1.0 mW, the average background subtracted values for four different bases were $N_s = (460.7 \pm 3.5)$ kHz, $N_i = (210.7 \pm 1.0)$ kHz and $N = (33.33 \pm 0.05)$ kHz. These are the values that also corresponds to the maximum counts shown in Figure 6. The calculated pair rates and the heralding efficiencies are plotted in Figure 7b. The pair rate from the V-basis at 1.0 mW was $R_{pair} = (2.92 \pm 0.12)$ MHz. Also, signal and idler heralding efficiencies of $\eta_s = 15.8\%$ and $\eta_i = 7.2\%$, respectively. The pair rate from all four bases showed a linear increase with increasing pump power, while the heralding efficiencies remained fairly constant as one would expect.

V. DISCUSSION AND OUTLOOK

The most significant advantage of our compensation method is its ability to effectively and easily compensate for both the spatial and temporal walk-off of photon fields at any wavelength. With our novel compensation method, the coincidence rate of signal and idler photons at 1.0 mW of pump power was $N = (33.33 \pm 0.05)$ kHz, showing a significant improvement from the coincidence rate observed without the compensation which was $N = (4.20 \pm 0.01)$ kHz. At the same power, the average entanglement visibility of $(96.6 \pm 0.3)\%$, and the average pair generation rate of (2.92 ± 0.12) MHz from all four bases were observed. The trends of all these bases in Figure 7b indicate that 100 MHz of pair rate could possibly be achieved at the power level of only around 50 mW, making it a promising source for long distance QKD [11]. With the validation from our experiment, we anticipate this compensation technique contributing not only to advancements in long-distance quantum networks but also to other practical quantum entanglement applications that require non-degenerate entangled photon pairs.

VI. ACKNOWLEDGEMENT

The authors acknowledge funding from the Natural Sciences and Engineering Research Council of Canada (NSERC), Canada Foundation for Innovation (CFI), Ontario Research Fund (ORF) and Canadian Space Agency (CSA). We thank Younseok Lee for assistance with the purchases of PPLN crystal and the CW laser. We thank Ramy Tannous and Henri Morin for assistance with handling equipments in the lab.

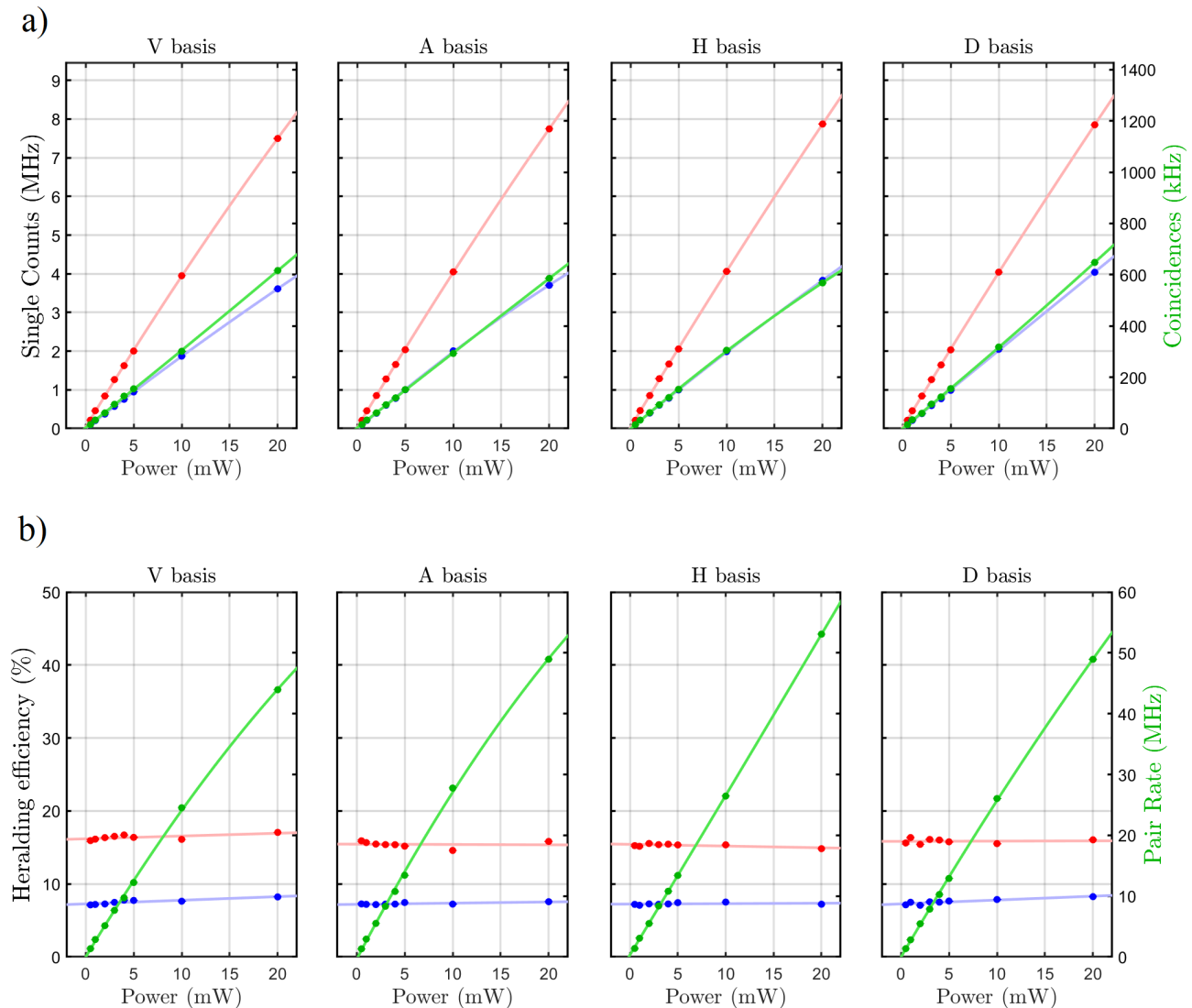


FIG. 7: The single counts of both signal (red) and idler (blue) photons, as well as the coincidence (green) counts are measured from four different polarization basis while varying the pump power. After the necessary background subtractions, the data are plotted on these graphs. Graphs showing the photon pair emission rates R_{pair} (green), along with the heralding efficiencies of the signal photon η_s (blue) and the idler photon η_i (red) for different pump powers, calculated from the data shown in (a).

-
- [1] Z. Tang, R. Chandrasekara, Y. C. Tan, C. Cheng, K. Durak, and A. Ling, The photon pair source that survived a rocket explosion (2015), arXiv:1512.08834 [physics.ins-det].
- [2] T. Kim, M. Fiorentino, and F. N. C. Wong, Phase-stable source of polarization-entangled photons using a polarization sagnac interferometer, Phys. Rev. A **73**, 012316 (2006).
- [3] R. Shimizu, T. Yamaguchi, Y. Mitsumori, H. Kosaka, and K. Edamatsu, Generation of polarization entanglement from spatially correlated photons in spontaneous parametric down-conversion, Phys. Rev. A **77**, 032338 (2008).
- [4] J. C. Chapman, C. C. Lim, and P. G. Kwiat, Hyperentangled time-bin and polarization quantum key distribution, Phys. Rev. Appl. **18**, 044027 (2022).
- [5] L. Shen, C. H. Chow, J. Y. X. Peh, X. J. Yeo, P. K. Tan, and C. Kurtsiefer, Distributing polarization-entangled photon pairs with high rate over long distances through standard telecommunication fiber, Physical Review Applied **18**, 10.1103/physrevapplied.18.044075 (2022).

- [6] J. S. Sidhu, S. K. Joshi, M. Gündoğan, T. Brougham, D. Lowndes, L. Mazzarella, M. Krutzik, S. Mohapatra, D. Dequal, G. Vallone, P. Villoresi, A. Ling, T. Jennewein, M. Mohageg, J. G. Rarity, I. Fuentes, S. Pirandola, and D. K. L. Oi, *Advances in space quantum communications, IET Quantum Communication* **2**, 182–217 (2021).
- [7] R. Ursin, F. Tiefenbacher, T. Schmitt-Manderbach, H. Weier, T. Scheidl, M. Lindenthal, B. Blauensteiner, T. Jennewein, J. Perdigues, P. Trojek, B. Ömer, M. Fürst, M. Meyenburg, J. Rarity, Z. Sodnik, C. Barbieri, H. Weinfurter, and A. Zeilinger, *Entanglement-based quantum communication over 144km*, *Nature Physics* **3**, 481–486 (2007).
- [8] M. Hentschel, H. Hübel, A. Poppe, and A. Zeilinger, *Three-color sagnac source of polarization-entangled photon pairs*, *Optics Express* **17**, 23153 (2009).
- [9] Z. Li, K. Xue, J. Li, L. Chen, R. Li, Z. Wang, N. Yu, D. S. L. Wei, Q. Sun, and J. Lu, *Entanglement-assisted quantum networks: Mechanics, enabling technologies, challenges, and research directions*, *IEEE Communications Surveys and Tutorials* **25**, 2133–2189 (2023).
- [10] X. Ma, C.-H. F. Fung, and H.-K. Lo, *Quantum key distribution with entangled photon sources*, *Physical Review A* **76**, 10.1103/physreva.76.012307 (2007).
- [11] J.-P. Bourgoin, E. Meyer-Scott, B. L. Higgins, B. Helou, C. Erven, H. Hübel, B. Kumar, D. Hudson, I. DSouza, R. Girard, R. Laflamme, and T. Jennewein, *A comprehensive design and performance analysis of low earth orbit satellite quantum communication*, *New Journal of Physics* **15**, 023006 (2013).
- [12] I. Esmaeil Zadeh, J. W. N. Los, R. B. M. Gourgues, V. Steinmetz, G. Bulgarini, S. M. Dobrovolskiy, V. Zwiller, and S. N. Dorenbos, *Single-photon detectors combining high efficiency, high detection rates, and ultra-high timing resolution*, *APL Photonics* **2**, 111301 (2017), https://pubs.aip.org/aip/app/article-pdf/doi/10.1063/1.5000001/14567918/111301_1.online.pdf.
- [13] M. Yang, S.-K. Liao, W.-S. Tang, W.-Q. Cai, Y. Li, J. Yin, and C.-Z. Peng, *In-orbit dark count rate performance and radiation damage high-temperature annealing of silicon avalanche photodiode single-photon detectors of the micus satellite*, *Opt. Express* **32**, 12601 (2024).
- [14] J. B. Abshire, X. Sun, H. Riris, J. M. Sirota, J. F. McGarry, S. Palm, D. Yi, and P. Liva, *Geoscience laser altimeter system (glas) on the icesat mission: On-orbit measurement performance*, *Geophysical Research Letters* **32**, <https://agupubs.onlinelibrary.wiley.com/doi/pdf/10.1029/2005GL024028>.
- [15] I. DSouza, J.-P. Bourgoin, B. L. Higgins, J. G. Lim, R. Tannous, S. Agne, B. Moffat, V. Makarov, and T. Jennewein, *Repeated radiation damage and thermal annealing of avalanche photodiodes*, *EPJ Quantum Technology* **8**, 10.1140/epjqt/s40507-021-00103-0 (2021).
- [16] D. Ribezzo, M. Zahidy, G. Lemmi, A. Petitjean, C. De Lazzari, I. Vagniluca, E. Conca, A. Tosi, T. Occhipinti, L. K. Oxenløwe, A. Xuereb, D. Bacco, and A. Zavatta, *Quantum key distribution over 100 km of underwater optical fiber assisted by a fast-gated single-photon detector*, *Phys. Rev. Appl.* **20**, 044052 (2023).
- [17] T. Jennewein, J. Bourgoin, B. Higgins, C. Holloway, E. Meyer-Scott, C. Erven, B. Heim, Z. Yan, H. Hübel, G. Weihs, E. Choi, I. D’Souza, D. Hudson, and R. Laflamme, *Qeysat: A mission proposal for a quantum receiver in space*, *Proceedings of SPIE - The International Society for Optical Engineering* **8997** (2014).
- [18] C. J. Pugh, S. Kaiser, J.-P. Bourgoin, J. Jin, N. Sultana, S. Agne, E. Anisimova, V. Makarov, E. Choi, B. L. Higgins, and T. Jennewein, *Airborne demonstration of a quantum key distribution receiver payload*, *Quantum Science and Technology* **2**, 024009 (2017).
- [19] *Qeysat mission - canadian space agency*, online source (last accessed in april 2024) : www.asc-csa.gc.ca/eng/satellites/qeysat.asp.
- [20] F. Steinlechner, P. Trojek, M. Jofre, H. Weier, D. Perez, T. Jennewein, R. Ursin, J. Rarity, M. W. Mitchell, J. P. Torres, H. Weinfurter, and V. Pruneri, *A high-brightness source of polarization-entangled photons optimized for applications in free space*, *Optics Express* **20**, 9640 (2012).
- [21] O. Gayer, Z. Sacks, E. Galun, and A. Arie, *Temperature and wavelength dependent refractive index equations for MgO-doped congruent and stoichiometric LiNbO₃*, *Applied Physics B: Lasers and Optics* **91**, 343 (2008).
- [22] D. N. Makarov, *Theory for the beam splitter in quantum optics: quantum entanglement of photons and their statistics, hom effect* (2022), arXiv:2211.03359 [quant-ph].
- [23] Y. Shi, S. Moe Thar, H. S. Poh, J. A. Grieve, C. Kurtsiefer, and A. Ling, *Stable polarization entanglement based quantum key distribution over a deployed metropolitan fiber*, *Applied Physics Letters* **117**, 10.1063/5.0021755 (2020).
- [24] Y. S. Lee, M. Xie, R. Tannous, and T. Jennewein, *Sagnac-type entangled photon source using only conventional polarization optics* (2020), arXiv:2007.05095 [quant-ph].
- [25] A. Lohrmann, C. Perumangatt, A. Villar, and A. Ling, *Broadband pumped polarization entangled photon-pair source in a linear beam displacement interferometer*, *Applied Physics Letters* **116**, 10.1063/1.5124416 (2020).
- [26] J. F. Clauser, M. A. Horne, A. Shimony, and R. A. Holt, *Proposed experiment to test local hidden-variable theories*, *Phys. Rev. Lett.* **23**, 880 (1969).
- [27] G. Peruzzo and S. Sorella, *Entanglement and maximal violation of the chsh inequality in a system of two spins j: A novel construction and further observations*, *Physics Letters A* **474**, 128847 (2023).